
Taming the Frequency Factory of Sinusoidal Networks

Tiago Novello*
IMPA

Diana Aldana*
IMPA

Luiz Velho
IMPA

Abstract

This work investigates the structure and representation capacity of *sinusoidal* MLPs, which have recently shown promising results in encoding low-dimensional signals. This success can be attributed to its *smoothness* and *high representation capacity*. The first allows the use of the network’s derivatives during training, enabling regularization. However, defining the architecture and initializing its parameters to achieve a desired capacity remains an empirical task. This work provides theoretical and experimental results justifying the capacity property of sinusoidal MLPs and offers control mechanisms for their initialization and training. We approach this from a Fourier series perspective and link the training with the model’s spectrum. Our analysis is based on a *harmonic expansion* of the sinusoidal MLP, which says that the composition of sinusoidal layers produces a large number of new frequencies expressed as integer linear combinations of the *input frequencies* (weights of the input layer). We use this novel identity to *initialize* the input neurons which work as a sampling in the signal spectrum. We also note that each hidden neuron produces the same frequencies with amplitudes completely determined by the hidden weights. Finally, we give an upper bound for these amplitudes, which results in a *bounding* scheme for the network’s spectrum during training.

1 Introduction

Implicit neural representations (INRs) have emerged as a powerful method to represent media objects, such as images and surfaces. They contrast with the classical techniques as they encode the data continuously on the parameters by mapping the coordinates to the signal values. For example, in the case of an image, an INR f receives a point (x, y) and returns the RGB value $f(x, y)$. In this case, the network’s domain is low-dimensional, which differs from classical machine learning representations, where the input is a discrete image. Another difference is that we would like the INR to fit the input data as close as possible, as in the problem of approximating signals using *radial basis functions*.

As noted by Tancik et al. [24], since *multilayer perceptrons* (MLPs) activated by ReLU cannot introduce high frequencies, they are not capable of representing detailed signals. To avoid getting stuck in a local minimum of the loss function where the INR does not contain high frequencies, they project the input coordinates onto a list of sines and cosines (*Fourier feature mapping*). This projection allows the INR to bypass the *spectral bias* [17] and represent detailed signals. In parallel, Sitzmann et al. [22] presented an initialization scheme for sinusoidal MLPs, which were considered difficult to train due to the initialization leading to undesirable local minima [14]. Their scheme ensures stability and convergence during training. An observation that partially justifies the representation power of a sinusoidal INR is that its first layer acts as a Fourier feature mapping [30].

Several works used sinusoidal INRs to represent images [30, 16], surfaces [27, 12], animation [10, 13], and radiance fields [2]. They have empirically demonstrated that such INRs have a high capacity to represent fine details. However, they also show well-known limitations [29], such as controlling the signal bandlimit and determining the appropriate parameters to efficiently represent a given signal.

*These authors contributed equally to this work.

This work considers an alternative approach for such problems through a novel *trigonometric identity* (Theorem 1) which resembles a *Fourier series* of a sinusoidal neuron. We use this formula to understand the network’s capacity by investigating how the layer’s composition compacts information. In addition, we explore practical issues of initialization in sinusoidal INRs providing a reinterpretation of SIREN’s scheme and ways of improving it. For this, we note that the expansion of each sinusoidal neuron produces a large number of new frequencies in terms of the first layer weights (*input frequencies*). We also prove that the corresponding amplitudes are bounded by a term depending only on the INR’s hidden weights (Theorem 2). Finally, we apply this result to control the bandlimit of the network spectrum during training. In summary, our contributions are:

- We present a trigonometric identity that says that each sinusoidal neuron *expands* as a wide sum of sines with its new frequencies being an integer linear combination of the input frequencies. The corresponding amplitudes are given by the hidden weights.
- We provide an *upper bound* for the amplitudes in the expansion of a sinusoidal neuron, which offers tools to control the resulting signal using the hidden weights.
- We use the trigonometric identity to *initialize* sinusoidal INRs. First, we initialize the input neurons using the fact that they determine the possible INR spectrum. Then, we initialize the hidden weights, taking into account that they determine the corresponding amplitudes.
- We use the amplitude’s upper bound to *control the bandlimit* of a sinusoidal INR. For this, we design schemes to bound the hidden weights during training. These boundings, along with the initialization generate frequencies progressively around the input frequencies.

2 Related works

Implicit neural representation (INRs). INR [26] is a trending topic in the machine learning community that is used to learn highly detailed signals in low-dimension domains. Current INR architectures use *Fourier feature mappings* [24] or *sinusoidal activation* functions [22] to bypass the *spectral bias* [17] common in ReLU multilayer perceptrons. The high representation capacity of sinusoidal INRs has motivated their use to represent a wide range of media objects. Examples include audio [6, 22], images [3, 23], face morphing [20], signed distance functions [21, 9, 22, 27, 12], displacement fields [28], surface animation [10, 13], multi-resolution signals [19, 9, 5, 25, 16], among others. Most of these works exploit the derivatives of sinusoidal INRs in the loss functions.

Initialization. Considering sinusoidal activation functions in neural networks is a classical problem [18]; however, these INRs have been regarded as difficult to train [14]. Sitzmann et al. [22] overcome this by presenting a specific initialization scheme that allows training *sinusoidal INRs*, avoiding instability and ensuring convergence. Despite these advances, in practice, the initialization of such INRs remains an empirical task. In this work, inspired by Fourier series theory, we present a novel initialization method that allows us to train INRs with bandlimit. Recently, several works have addressed the representation problem of sinusoidal INRs from different perspectives. Zell et al. [30] approached this problem by observing that the first layer of a sinusoidal INR is similar to a Fourier feature mapping. Here, in addition to improving the initialization of sinusoidal INRs, we present a training scheme for bounding the spectra of these networks.

Control of spectrum. One of the main drawbacks of sinusoidal INRs is the lack of frequency control. Sitzmann et al. [22] addressed this issue by multiplying the input frequencies by a factor ω_0 to scale them to an appropriate range. However, even an appropriate choice of ω_0 could result in a noisy reconstruction since we have no control guarantees over the network spectrum. We avoid the ω_0 problem by providing a novel initialization for the first layer. This is inspired by the fact that the frequencies generated by the network are determined by the input layer. Additionally, we provide a bounding scheme during training considering that the hidden layers define the frequency amplitudes. Other works [9, 5] employed *multiplicative filter networks* (MFNs) [7] to control the bandlimit by applying a filter over the spectrum. However, this strategy is prone to introducing reconstruction artifacts. It is important to note that MFNs are fundamentally different from neural networks as they are not modeled by the composition of sinusoidal layers, which is the focus of this work.

3 A Fourier series interpretation of sinusoidal INRs

This work addresses the problem of obtaining an *efficient initialization* and a *training scheme* with controlled bandlimit for the frequencies of sinusoidal INRs. This section presents the mathematical definitions and some novel formulas for approaching such tasks.

Sinusoidal INRs demonstrated a high representational capacity with only a few hidden layers [22, 30, 19]. Thus, to understand how the composition of its layers are compacting the information, we propose to investigate a sinusoidal INR $f : \mathbb{R}^d \rightarrow \mathbb{R}$ consisting of a single hidden layer $\mathbf{S} : \mathbb{R}^m \rightarrow \mathbb{R}^n$, with $m, n \in \mathbb{N}$. Specifically, we consider f to be expressed as $f(\mathbf{x}) = \mathbf{L} \circ \mathbf{S} \circ \mathbf{D}(\mathbf{x})$, with $\mathbf{S}(\mathbf{x}) = \sin(\mathbf{W}\mathbf{x} + \mathbf{b})$, where $\mathbf{W} \in \mathbb{R}^{n \times m}$ is the hidden matrix, and $\mathbf{b} \in \mathbb{R}^n$ the bias. The *input layer* $\mathbf{D}(\mathbf{x}) = \sin(\omega\mathbf{x} + \varphi)$ projects the input \mathbf{x} into a list of harmonics (*input neurons*) $D_i(\mathbf{x}) = \sin(\omega_i\mathbf{x} + \varphi_i)$ with *frequencies* $\omega = (\omega_1, \dots, \omega_m) \in \mathbb{R}^{m \times d}$ and *shifts* $\varphi \in \mathbb{R}^m$. Finally, $\mathbf{L}(\mathbf{x}) = \mathbf{C}\mathbf{x} + d$ is a linear layer. We show empirically that such architecture has enough capacity for our purposes.

We now present some properties of the sinusoidal layers, which play key roles in the representation, and give a reinterpretation of them in terms of the network parameters. First, note that the *hidden neurons* $\mathbf{h}(\mathbf{x}) := \mathbf{S} \circ \mathbf{D}(\mathbf{x})$ are defined by composing the dictionary \mathbf{D} with the hidden sinusoidal layer which results in a list with elements $h_i(\mathbf{x}) = \sin\left(\sum_{j=1}^m W_{ij} \sin(\omega_j\mathbf{x} + \varphi_j) + b_i\right)$.

We now present a key result of this work, which states that we can linearize a hidden neuron by a sum of sines with frequencies and amplitudes completely determined by ω and \mathbf{W} .

Theorem 1. *Each neuron h_i of a sinusoidal INR has an amplitude-phase expansion of the form*

$$h_i(\mathbf{x}) = \sum_{\mathbf{k} \in \mathbb{Z}^m} \alpha_{\mathbf{k}} \sin(\beta_{\mathbf{k}}\mathbf{x} + \lambda_{\mathbf{k}}), \quad \text{where } \beta_{\mathbf{k}} = \sum_j k_j \omega_j, \quad \lambda_{\mathbf{k}} = \sum_j k_j \varphi_j + b_i, \quad (1)$$

and $\alpha_{\mathbf{k}} = \prod_{j=1}^m J_{k_j}(W_{ij})$ is the product of the Bessel functions of the first kind.

The Bessel functions J_k appear in the Fourier series of $\sin(a \sin(x))$ [1, Page 361] and Theorem 1 is a generalization of this result. The complete proof and details can be found in Appex A, and Appex D gives a generalization for more hidden layers.

We list some consequences of (1). First, the layer composition introduces a wide number of frequencies $\beta_{\mathbf{k}}$ depending only on ω , and shifts given by the input shift φ and the hidden bias \mathbf{b} . Precisely, truncating the expansion by summing over $|\mathbf{k}|_{\infty} \leq B \in \mathbb{N}$,² implies that each neuron h_i could learn $\frac{(2B+1)^m - 1}{2}$ non-null frequencies. This *frequency factory* explains why composing sinusoidal layers *may* compact data information. Indeed, Fig 1 shows that training with fewer parameters using a narrow sinusoidal INR with one hidden layer performs better than a wide INR with no hidden layer. Additionally, we explore this factory to present an initialization of the INR’s input neurons in Sec 4.1.

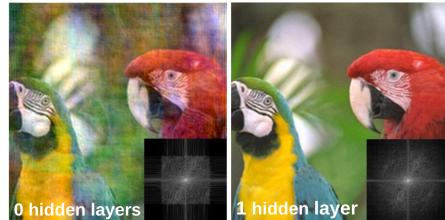


Figure 1: Comparison between INRs with zero and one hidden layers. Training with one hidden layer is significantly faster (50s vs 13m), uses half the parameters (33842 vs 67803), and produces higher quality results (34.4dB vs 21.1dB).

Secondly, note that the weights \mathbf{W} fully determine the amplitude $\alpha_{\mathbf{k}}$ of each harmonic $\sin(\beta_{\mathbf{k}}x + \lambda_{\mathbf{k}})$ in the expansion. Additionally, we can derive the corresponding *sine-cosine form* of (1),

$$h_i(\mathbf{x}) = \sum_{\mathbf{k} \in \mathbb{Z}^m} A_{\mathbf{k}} \sin(\beta_{\mathbf{k}}\mathbf{x}) + B_{\mathbf{k}} \cos(\beta_{\mathbf{k}}\mathbf{x}), \quad \text{with } A_{\mathbf{k}} = \alpha_{\mathbf{k}} \cos(\lambda_{\mathbf{k}}), \quad B_{\mathbf{k}} = \alpha_{\mathbf{k}} \sin(\lambda_{\mathbf{k}}). \quad (2)$$

Note that the generated frequencies are independent of the index i , thus the hidden neurons share the same harmonics: $\sin(\beta_{\mathbf{k}}\mathbf{x})$, $\cos(\beta_{\mathbf{k}}\mathbf{x})$. Since different linear combinations of the input frequencies may correspond to a single generated frequency, (2) isn’t (yet) the Fourier transform of the network’s output. In other words, we could have two integer vectors $\mathbf{k}, \mathbf{l} \in \mathbb{Z}^m$ such that $\beta_{\mathbf{k}} = \beta_{\mathbf{l}}$. In Appex B, we show how to aggregate those frequencies to obtain the final Fourier transform.

² $|\mathbf{k}|_{\infty}$ denotes $\max\{|k_1|, \dots, |k_m|\}$.

A natural issue regarding the frequency factory is the existence of $B > 0$ such that $|\alpha_{\mathbf{k}}|$ is small for $|\mathbf{k}|_{\infty} \geq B$. We can use the formula of $\alpha_{\mathbf{k}}$ to determine a bounding, showing that if $|\mathbf{W}|_{\infty} < 2$ then the coefficients $A_{\mathbf{k}}$ and $B_{\mathbf{k}}$ decay exponentially as $|\mathbf{k}|_{\infty}$ grows.

Theorem 2. *The magnitude of the amplitude $\alpha_{\mathbf{k}}$ is bounded by $\prod_{j=1}^m \left(\frac{|W_{ij}|}{2}\right)^{|k_j|} \frac{1}{|k_j|!}$.*

Sec 4.2 presents a bandlimit control mechanism during training based on Theorem 2.

4 Initialization and frequency bounding

This section presents an *initialization* and *frequency control* schemes for sinusoidal INRs. Our initialization considers integer input frequencies (based on a Fourier series interpretation) and uses Theorem 1 to study the spectral content of layer composition. Then, we use Theorem 2 to control the bandlimit of sinusoidal INRs during training.

4.1 Initializing the input layer is a sampling in the spectral domain

First, we initialize ω with *integer frequencies* by setting $\omega_j \in \frac{2\pi}{p}\mathbb{Z}^d$ and freezing them during training, where $p \in \mathbb{R}^+$ will be the INR’s *period*. This guarantees that the input neurons \mathbf{D} are p -periodic. Then, Theorem 1 ensures that such periodicity is preserved by the layer activation. On the right, we show a comparison between SIREN and our initialization with $p = 2$, both supervised only inside the red square (image from [4]). This gives a proof of the empirical results about periodicity in [30]. Additionally, (2) implies that we can rewrite the INR as:

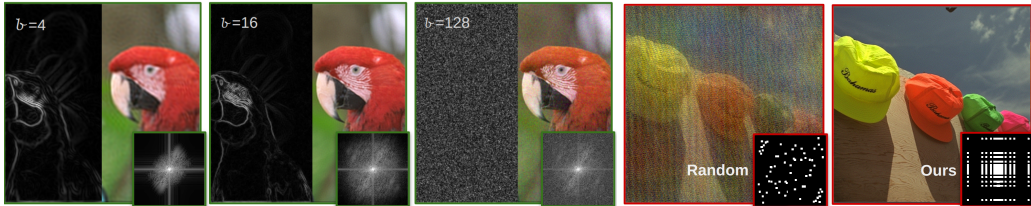
$$f(\mathbf{x}) = \sum_{\mathbf{k} \in \mathbb{Z}^m} \langle \mathbf{C}, A_{\mathbf{k}} \rangle \sin(\beta_{\mathbf{k}} \mathbf{x}) + \langle \mathbf{C}, B_{\mathbf{k}} \rangle \cos(\beta_{\mathbf{k}} \mathbf{x}) + d \quad (3)$$

Since the generated frequencies $\beta_{\mathbf{k}}$ only depend on the frozen parameters ω , the training is responsible for learning the amplitudes of the sine-cosine series in (3).

Assume that the ground truth has a bandlimit B . First, note that we can sample ω directly on the cube $[-B, B]^d$, since (3) indicates that the chosen frequencies appear in the spectrum of f . However, it also shows that the composition of layers produces an exponential number of new frequencies. These may extrapolate the cube since they are integer combinations of the input frequencies. Therefore, we propose to sample ω_j in $\frac{2\pi}{p}[-\ell, \ell]^d$, with $0 < \ell < B$ a *bandlimit* for the input frequencies. Indeed, as the hidden matrix \mathbf{W} is initialized with small values ($|W_{ij}| < 2$, see Sec 4.2), the magnitudes of $A_{\mathbf{k}}$ and $B_{\mathbf{k}}$ decrease as $|\mathbf{k}|_{\infty}$ increases. This is a consequence of Theorem 2:

$$|\alpha_{\mathbf{k}}| \leq \prod_{j=1}^m \frac{\left(\frac{|W_{ij}|}{2}\right)^{|k_j|}}{|k_j|!} \leq \frac{1}{|k_1|! \dots |k_m|!} \quad \text{for } i = 1, \dots, n. \quad (4)$$

Thus, the generated frequencies $\beta_{\mathbf{k}}$ with small \mathbf{k} have more influence over the expansion (3), mimicking Fourier series theory. This motivates us to initialize the input frequencies close to the origin; we found $\ell = \frac{B}{3}$ to work well with the experiments. Fig 3a shows that it is necessary, as higher ℓ introduces noise. However, in next section we avoid this problem by bounding the INR’s spectrum.



(a) Reconstruction of an image with bandlimit $B = 128$. (b) Random initialization of ω and ours.
Figure 3: Training with varying maximum input frequencies (a) and the distribution of ω (b).

Note that if ω_j is an input frequency, $-\omega_j$ is also present in the initialization. This is a consequence of $\sin(\omega_j \mathbf{x} + \varphi_j) = \cos(\varphi_j) \sin(\omega_j \mathbf{x}) - \sin(\varphi_j) \sin(-\omega_j \mathbf{x} + \pi/2)$ being a linear combination of harmonics with frequencies $\omega_j, -\omega_j$. Then, we only need to sample ω_j in half of the cube $[-\ell, \ell]^d$. Also, from (3) we have that the final bias d represents the amplitude of the frequency $(0, 0)$, hence we do not initialize it in ω . Finally, since $\mathbf{D}(\mathbf{x}) = \sin(\omega \mathbf{x} + \varphi)$, we initialize φ uniformly in $[-\frac{\pi}{2}, \frac{\pi}{2}]$.

We now discuss an initialization of the frequencies $\omega \in \mathbb{R}^{m \times d}$. First, note that (4) indicates that only frequencies $\beta_{\mathbf{k}}$ with \mathbf{k} small can have high amplitudes. Then we initialize ω such that it determines a sampling on the spectral domain.

Specifically, we split $[-\ell, \ell]^d$ in regions $\mathbf{L} = [-\ell, \ell]^d$ of *low* and $\mathbf{H} = [-\ell, \ell]^d \setminus \mathbf{L}$ of *high* frequencies, $\ell \in (0, \ell)$. When $\omega_j \in \mathbf{L}$, small variations in k_j results in a frequency near $\beta_{\mathbf{k}}$. Indeed, Fig 4b shows how low frequencies (green square) introduce frequencies around the input frequencies (Fig 4a). On the other hand, if $\omega_j \in \mathbf{H}$ then $\beta_{\mathbf{k}+\mathbf{e}_j}$ is far away from $\beta_{\mathbf{k}}$; we observe this in Fig 4b-e, where ω_j is the red point and the arrows show the generated frequencies $k_j \omega_j$.

When sampling frequencies in \mathbf{L} , we include $(1, 0)$ and $(0, 1)$. This guarantees that any frequency could be generated and prevents the appearance of sub-periods (see Appex C). Fig 5 shows an example in which this condition is violated, leading to an unappropriated reconstruction. For the higher frequencies in \mathbf{H} , we sample in a grid-like fashion, uniformly covering the half square \mathbf{K} .



Figure 5: Choosing ω as the cartesian product of the odd frequencies w/o $(1, 0), (0, 1)$.

4.2 Frequency bounding and hidden layer initialization

Sinusoidal INRs can represent detailed signals due to the exponential number of frequencies generated by the sine activation. However, they could manifest as noise in the reconstruction. Here, we use Theorem 2 to introduce a *bounding* scheme to control the INR bandlimit during training. Then, we use the relationship between the hidden matrix \mathbf{W} , generated frequencies $\beta_{\mathbf{k}}$, and ω to define the *bounding by blocks*. Next, we initialize \mathbf{W} in a range defined by the bounds, improving performance. Finally, we define a new architecture that allows us to learn the bounds. Precisely, using Theorem 2, we have that the amplitudes of the generated frequencies are limited by:

$$|\alpha_{\mathbf{k}}| \leq \left(\frac{\|\mathbf{W}_i\|_{\infty}}{2} \right)^{|\mathbf{k}|_1} \frac{1}{\prod_{j=1}^m |k_j|!}. \quad (5)$$

This implies that if $\|\mathbf{W}\|_{\infty} \leq 2$ then the amplitude of a generated frequency $\beta_{\mathbf{k}}$ rapidly decreases when the coordinates of \mathbf{k} grow. Thus, forcing $\|\mathbf{W}\|_{\infty} \leq 2$ during training reduces the appearance of $\beta_{\mathbf{k}}$ with high $|\mathbf{k}|_{\infty}$ in the reconstruction. Therefore, we use (5) to define a *bounding* scheme that controls the INR bandlimit so that the generated frequencies saturate around small multiples of the input frequencies. It simply clamps the coefficients W_{ij} by a *bound* parameter $c \in (0, 2]$. This procedure is applied at each epoch, enforcing $\|\mathbf{W}\|_{\infty} \leq c$. Fig 6 presents the results of bounding $\|\mathbf{W}\|$ with different bounds c .



Figure 6: Training for 6000 epochs with $\ell = 30$ and bounds $c=0.1, 0.2, 0.5$. The bound over the spectrum restricts the appearance of high frequencies.

We initialize \mathbf{W} with values in $[-c, c]$ using a normal distribution with mean 0 and standard deviation $\frac{c}{3}$. Observe that SIREN [22] also controls the bandlimit but only at initialization, since the weights of \mathbf{W} are sampled in $(-\sqrt{6/m}, \sqrt{6/m})$. In other words, since $|\mathbf{W}|_\infty < 2$ (for $m > 1$) at initialization, they do not introduce high frequencies at the beginning of the training. Additionally, we note a faster convergence when training with bounding using our initialization (see Appex E.2).

In Sec 4.1 we split the input frequencies ω in two sets: the low ($|\omega_j|_\infty \leq \ell$) and high ($|\omega_j|_\infty > \ell$) frequencies. Now, observe that each input frequency ω_j is associated with the j -column of \mathbf{W} . Then, by bounding the weights of \mathbf{W} related to high frequencies, we restrict the amplitudes of β_k that could exceed the Nyquist limit B . Conversely, since low frequencies are used to span around ω , we consider a higher bounding for their columns. Precisely, we define two parameters c_1 and c_2 to bound the weights W_{ij} corresponding to ω_j in \mathbf{L} and \mathbf{H} , respectively,

$$|\omega_j|_\infty \leq \ell \rightarrow W_{ij} = \text{clamp}(W_{ij}, [-c_1, c_1]); \quad |\omega_j|_\infty > \ell \rightarrow W_{ij} = \text{clamp}(W_{ij}, [-c_2, c_2]).$$

Analogously, we initialize \mathbf{W} such that each column is normal distributed with mean 0 and standard deviation $\frac{c_l}{3}$, with c_l the bound corresponding to that column.

Finally, we present a scheme to *learn the bounding* parameters c_j during training. For this, we bound each j -column W_{*j} of the hidden matrix \mathbf{W} using a tanh activation followed by multiplication with a trainable bounding parameter c_j , that is, $\tanh(W_{*j})c_j$. Clearly, the resulting column is bounded by c_j . In other words, we are replacing the hidden layer $\sin(\mathbf{W}\mathbf{x} + \mathbf{b})$ by

$$\sin(\tanh(\mathbf{W})\mathcal{C}\mathbf{x} + \mathbf{b}) \text{ where } \mathcal{C} \text{ is a diagonal matrix with each } jj\text{-entry being } c_j. \quad (6)$$

To prevent the bounds from getting too big, we use Theorem 2 to define a regularization $\mathcal{L}_{\text{reg}} = \sum |c_j|$. Otherwise, the hidden weights virtually grow unbounded and the INR overfits as in the usual training.

5 Additional experiments and comparisons

This section presents experiments regarding the initialization and bounding of frequencies of an INR f . Our code is based on the MRNet [16] repository, using the images of the Kodak dataset resized to $[-1, 1]^2$. Since our architecture is determined by the hidden matrix $\mathbf{W} \in \mathbb{R}^{n \times m}$, we use n and m to define f . We initialize the network using the scheme given in Sec 4.1. We use Adam’s optimizer [8] with a fixed learning rate $1e-4$. For the quantitative evaluations, we use the mean and standard deviation of the PSNR evaluated on the test set (10% random pixels). Besides comparing the reconstruction quality of our INR f , we also evaluate the resulting analytical gradient ∇f to show that our method adds high order regularity in the signal reconstruction. All experiments were performed in a GPU NVIDIA TITAN X (Pascal) with 12 GB.

5.1 Initialization

First, we compare our ω initialization against the uniform distribution. We obtained a 4dB improvement of PNSR on average (with a std of 1.6dB). We also present an ablation over the parameter ℓ which splits the square $[-\ell, \ell]^2$ in regions of low (\mathbf{L}) and high (\mathbf{H}) frequencies (see Sec 4.1). Here we consider $\ell = 85$ and $\ell = 21, 42, 64$, and sample ω with 30%, 50%, and 70% of coordinates in \mathbf{H} . Table 1 shows the performance of the INR, with the signal (grad.) mean std of 1.9dB (3.1dB).

This experiment considered all the images in the dataset. Observe that all values of the row $\ell = 64$ have less PSNR, showing that an INR with very high frequencies performs worse even for small percentages (30%). Similarly, the performance worsens when we increase the number of high frequencies (last column).

	30%		50%		70%	
ℓ	Signal	Grad	Signal	Grad	Signal	Grad
21	35.2	26.9	35.2	26.6	35.0	26.0
42	35.1	26.3	34.8	24.6	33.8	22.2
64	34.2	25.2	33.3	21.6	30.8	15.0

Table 1: Training an INR with $176K$ params. for 400 epochs. Results indicate that it is better to sample more $\omega_j \in \mathbf{L}$ and choose a smaller ℓ .



Figure 7: Reconstructions with large ℓ present artifacts (overfitting) on the 10% unsupervised points.

We now test the influence of high frequencies by training an INR of size $m = 360$, $n = 512$ with $\ell = 256$ over 90% of the ground truth pixels. We vary the parameter $\ell = 60, 120, 220$ that defines low frequencies. Increasing the number of higher frequencies, the INR suffers from noise and overfitting. This can be noted in the reconstruction on the unsupervised pixels and gradients in Fig 7.

5.2 Bounding

In Sec 4.2 we presented a scheme to bound the INR spectrum. Here, we show additional experiments to demonstrate that this improves the signal and has a great benefit over the unsupervised gradient reconstruction. Then, we give a comparison between our fixed and trained bounding schemes.

Fig 8 shows a comparison between wo/w our bounding scheme to reconstruct an image of size 512^2 . To demonstrate the impact of our scheme, we sample the input frequencies using $\ell = 256$ and $\ell = 100$. Without bounding (left), we effectively reconstruct the signal at the supervised pixels (30.8 dB), but it results in a noisy gradient (15.8 dB). That is, we are overfitting the signal. On the other hand, when bounding the hidden weights, we observe significant improvements in both the signal (35.1 dB) and its gradient (27.8 dB). Our bounding scheme acts like a filter in both signal and gradient reconstruction.



Figure 8: Comparison of training wo/w bounds. Observe that training using bounds preserves high order information of the signal.

We perform a quantitative comparison, varying the parameters ℓ and c_2 , to numerically test our scheme on the dataset. Table 2 shows an improvement in the signal for all cases. Furthermore, the unsupervised gradient of the image is better learned when using bounds, showing an average increase of 9.6dB against the standard training. Also, the last two lines of the table show the impact of the parameters c_1, c_2 over the signal and gradient reconstructions. We consider training with $c_1 > c_2$ since we are prioritizing low input frequencies in the spectrum generation. Otherwise, this may imply a generation of high frequencies, possibly bypassing the Nyquist limit and resulting in a worse gradient reconstruction.

ℓ	c_1	c_2	signal		grad	
			NB	WB	NB	WB
256	1.5	0.05	32.6	34.8	14.5	25.8
190	1.5	0.05	34.0	35.9	18.5	26.1
190	1.5	0.2	34.0	34.4	18.5	21.0

Table 2: Training using our bounding scheme (WB) improves the signal and grad. reconstruction. The choice of c_2 greatly impacts the grad. fidelity. The std of the difference between each image signal (grad) quality wo/w bounding (NB) is 1.4dB (1.6dB) on average. Evaluations performed on the test set (10% of pixels).

Next, we show how we can learn each bound c_j . As described in Sec 4.2, we can incorporate a learnable c_j for each j -column of the hidden matrix through a modified layer (6). Fig 9 shows a comparison between our fixed bound scheme using initial un-tuned $c_1=1.0$ and $c_2=0.6$ (left) and the learned bound scheme (middle).



Figure 9: Comparison of training with fixed/learned bounds. Learning the bound of each frequency allows an adjustment of the signal spectrum resulting in better signal/gradient reconstructions. Each blue point in the diagram represents a pair (ω_j, c_j) .

As expected, training lowers the bounds for high frequencies (**H**) while maintaining or increasing the bounds of low frequencies (**L**). Thus, we achieve better reconstruction in both the signal and gradient. In Fig 6 (right), we note that low frequencies (left of the green line) have significant bounds, showing their importance during training. Conversely, the bounds of frequencies in **H** rapidly decrease as they grow higher. These schemes allow us to initialize with higher frequencies than $B/3$, accelerating convergence.

5.3 Comparisons

We first compare our method with SIREN, which requires choosing the frequency parameter ℓ ,³ a critical and often empirical task. Our approach uses ℓ to control the generation of new frequencies. To demonstrate this, we perform a comparison by varying ℓ as well as the number of input (m) and hidden (n) neurons. First, consider the case where we have no information about the bandlimit of the underlying signal and can only rely on the Nyquist limit B . Fig 10 presents a comparison between SIREN (1° row) and our method (2° row) with $\ell = B$. Note that SIREN produces very noisy reconstructions during training, while ours learns faster and does not suffer from noise. This is due to our bounding scheme, which limits the generation of high frequencies and provides more control during training (Sec 4.2). In contrast, SIREN initializes its parameters such that the spectrum is initially bounded but does not maintain this guarantee during training.

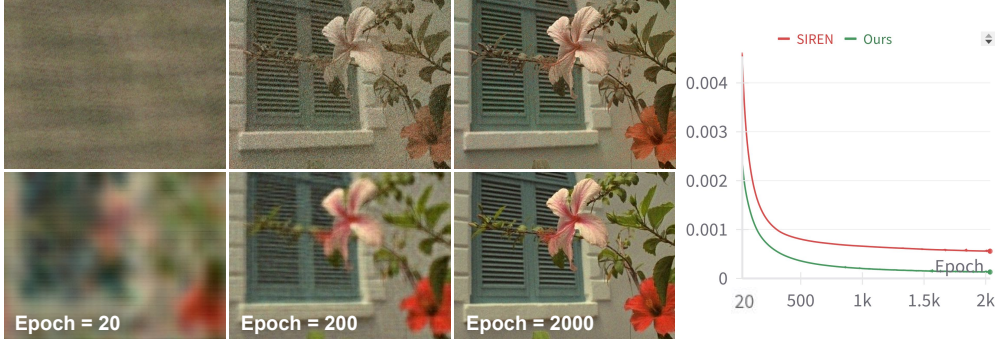


Figure 10: Comparing SIREN (1° row) with our method (2° row) when we only know the Nyquist limit. Note that SIREN introduces high frequencies at the beginning of training, resulting in very noisy reconstructions. Conversely, ours starts training low frequencies, obtaining a faster convergence.

Next, we consider a tuned ℓ for SIREN to show that even under this condition, our method provides a better training scheme for sinusoidal INRs. Fig 11 presents the comparison varying the number of input (m) and hidden (n) neurons. We consider the cases $m < n$ (1° row) and $m > n$ (2° row). Note that in both cases, our method performs better in the signal/gradient reconstructions. Also, we observe more robust training using our scheme, as seen in the loss functions in the 3° column.

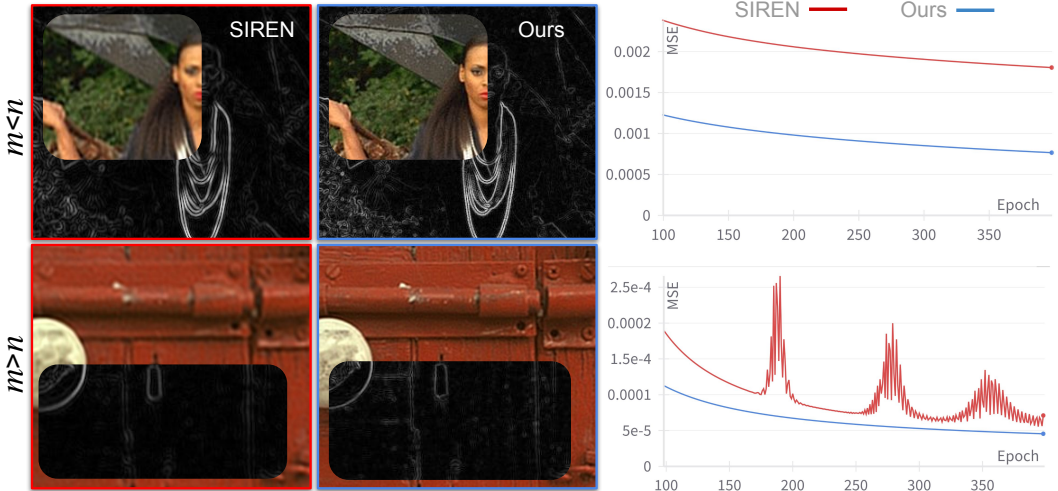


Figure 11: Comparison with SIREN considering $\ell = 40$. When there are more frequencies ($m > n$) our method converges faster (3° column, above), and we observe more training stability when $m < n$.

The experiments above showed that initializing SIREN with a high bandlimit ($\ell = B$) results in overfitting (Fig 10). Conversely, our method effectively learned the lower frequencies first

³Denoted as ω_0 in [22].

and performed better than SIREN with the same configuration and a tuned ℓ (Fig 11). Next, we numerically evaluate these experiments, providing a quantitative comparison with SIREN and BACON on the Kodak dataset. We compare different architectures (m, n) and spectrum bandlimits ℓ , evaluating the results in terms of signal and gradient PSNR over the supervised (Train) and unsupervised (Test) pixels. Table 3 presents these evaluations. As expected, SIREN performs well with $\ell = \frac{B}{3}$. In this case, our method is perceptually similar to SIREN but improves gradient reconstruction and consistently outperforms BACON. When $\ell = 171$, our method demonstrates the best quality in both signal and gradient, showing greater robustness to spectral noise and superior performance even with $\ell \geq B/3$. Finally, with $\ell = 256$, our method surpasses SIREN in all cases. For BACON, our method achieves better signal reconstruction, with comparable gradients. However, the following experiment shows that BACON’s reconstruction has visible defects in this scenario. Note that we do not supervise the training with gradient information.

ℓ	(m, n)	Train						Test					
		Signal			Gradient			Signal			Gradient		
		SIREN	BACON	Ours	SIREN	BACON	Ours	SIREN	BACON	Ours	SIREN	BACON	Ours
85	(1028,162)	32.9	-	32.9	26.5	-	28.8	31.9	-	32.2	25.5	-	28.2
	(416,416)	34.0	26.4	34.3	27.7	22.4	28.9	32.9	25.4	33.4	27.1	22.3	28.4
	(80,2024)	32.2	-	33.1	26.6	-	28.5	31.3	-	32.3	26.0	-	28.0
171	(1028,162)	31.3	-	33.9	22.0	-	27.2	22.9	-	32.9	20.7	-	26.8
	(416,416)	29.2	29.3	34.4	17.4	26.7	27.0	26.79	26.2	33.1	16.2	26.3	26.4
	(80,2024)	26.6	-	30.8	14.2	-	22.6	23.8	-	29.5	13.8	-	21.3
256	(1028,162)	26.8	-	33.3	12.8	-	24.7	24.1	-	31.9	12.7	-	23.9
	(416,416)	24.7	27.7	41.2	12.9	24.2	23.0	22.3	22.7	33.2	13.2	22.8	21.2
	(80,2024)	25.1	-	30.0	13.0	-	15.2	24.1	-	27.1	13.1	-	14.6

Table 3: Comparison between SIREN, BACON, and our method. We use several architectures (m, n) , bandlimits (ℓ) , and evaluate over the train (90%) and test(10%) sets of signal/gradient.

Lastly, Fig 12 presents a qualitative comparison between our bounding scheme and BACON. We consider the three initial bandlimits $\ell = 85, 171, 256$ as in Table 3. We note that BACON truncates the spectrum in a similar way as the 0 hidden layer INR (see Fig 1), resulting in ringing artifacts. Moreover, observe that it presents a loss of contrast as the bandlimit increases. Conversely, ours operates as a soft filter providing better reconstructions in all cases.



Figure 12: Comparison between BACON (red) and our method (blue), trained with different bandlimits $\ell = 85, 171, 256$. We observe that BACON uses a box filter, generating ringing artifacts (first image). In contrast, our method resembles a soft filter, improving quality.

6 Conclusions and limitations

We presented a study based on Fourier theory for sinusoidal INRs and used it to propose new schemes for both initialization and spectral control. Positively, our theoretical contributions generalize to different domains and aim to provide a better understanding of sinusoidal INRs for all applications. While we limited our experiments to images to demonstrate our theoretical claims; future works include using our schemes for other signals. We also have focused our studies on a single hidden layer architecture leaving the investigation of deep architectures for a follow-up work. In that sense, we are certainly considering future research aiming to extrapolate our results to general architectures and domains. Thus, we consider this work as a first step to unravel the powerful expressiveness of sinusoidal INRs.

References

- [1] Milton Abramowitz and Irene A Stegun. *Handbook of mathematical functions with formulas, graphs, and mathematical tables*, volume 55. US Government printing office, 1964.
- [2] Eric R Chan, Marco Monteiro, Petr Kellnhofer, Jiajun Wu, and Gordon Wetzstein. pi-gan: Periodic implicit generative adversarial networks for 3d-aware image synthesis. In *Proceedings of the IEEE/CVF conference on computer vision and pattern recognition*, pages 5799–5809, 2021.
- [3] Yinbo Chen, Sifei Liu, and Xiaolong Wang. Learning continuous image representation with local implicit image function. In *Proceedings of the IEEE/CVF conference on computer vision and pattern recognition*, pages 8628–8638, 2021.
- [4] M. Cimpoi, S. Maji, I. Kokkinos, S. Mohamed, , and A. Vedaldi. Describing textures in the wild. In *Proceedings of the IEEE Conf. on Computer Vision and Pattern Recognition (CVPR)*, 2014.
- [5] Yishun Dou, Zhong Zheng, Qiaoqiao Jin, and Bingbing Ni. Multiplicative fourier level of detail. In *Proceedings of the IEEE/CVF Conference on Computer Vision and Pattern Recognition*, pages 1808–1817, 2023.
- [6] Emilien Dupont, Adam Golinski, Milad Alizadeh, Yee Whye Teh, and Arnaud Doucet. Coin: Compression with implicit neural representations. In *International Conference on Learning Representations*, 2021. URL <http://arxiv.org/abs/2103.03123v2>.
- [7] Rizal Fathony, Anit Kumar Sahu, Devin Willmott, and J Zico Kolter. Multiplicative filter networks. In *International Conference on Learning Representations*, 2020.
- [8] Diederik P Kingma and Jimmy Ba. Adam: A method for stochastic optimization. *arXiv preprint arXiv:1412.6980*, 2014.
- [9] David B Lindell, Dave Van Veen, Jeong Joon Park, and Gordon Wetzstein. Bacon: Band-limited coordinate networks for multiscale scene representation. In *Proceedings of the IEEE/CVF conference on computer vision and pattern recognition*, pages 16252–16262, 2022.
- [10] Ishit Mehta, Manmohan Chandraker, and Ravi Ramamoorthi. A level set theory for neural implicit evolution under explicit flows. In *European Conference on Computer Vision*, pages 711–729. Springer, 2022.
- [11] L.J. Mordell. *Diophantine equations: Diophantine Equations*. ISSN. Elsevier Science, 1969. ISBN 9780080873428. URL <https://books.google.com.br/books?id=QugvF7xfE-oC>.
- [12] Tiago Novello, Guilherme Schardong, Luiz Schirmer, Vinicius da Silva, Helio Lopes, and Luiz Velho. Exploring differential geometry in neural implicits. *Computers & Graphics*, 108:49–60, 2022.
- [13] Tiago Novello, Vinicius da Silva, Guilherme Schardong, Luiz Schirmer, Helio Lopes, and Luiz Velho. Neural implicit surface evolution. In *Proceedings of the IEEE/CVF International Conference on Computer Vision*, pages 14279–14289, 2023.
- [14] Giambattista Parascandolo, Heikki Huttunen, and Tuomas Virtanen. Taming the waves: sine as activation function in deep neural networks. 2016.
- [15] RB Paris. An inequality for the bessel function $j_\nu(\nu x)$. *SIAM journal on mathematical analysis*, 15(1):203–205, 1984.
- [16] Hallison Paz, Daniel Perazzo, Tiago Novello, Guilherme Schardong, Luiz Schirmer, Vinicius da Silva, Daniel Yukimura, Fabio Chagas, Helio Lopes, and Luiz Velho. Mr-net: Multiresolution sinusoidal neural networks. *Computers & Graphics*, 2023.
- [17] Nasim Rahaman, Aristide Baratin, Devansh Arpit, Felix Draxler, Min Lin, Fred Hamprecht, Yoshua Bengio, and Aaron Courville. On the spectral bias of neural networks. In *International Conference on Machine Learning*, pages 5301–5310. PMLR, 2019.
- [18] E. Romero, J. Sopena, R. Alquézar, and J. Moliner. Neural networks with periodic and monotonic activation functions: a comparative study in classification problems. Feb 2000. URL <http://hdl.handle.net/2117/85060>.
- [19] Vishwanath Saragadam, Jasper Tan, Guha Balakrishnan, Richard G Baraniuk, and Ashok Veeraraghavan. Miner: Multiscale implicit neural representation. In *European Conference on Computer Vision*, pages 318–333. Springer, 2022.

- [20] Guilherme Schardong, Tiago Novello, Daniel Perazzo, Hallison Paz, Iurii Medvedev, Luiz Velho, and Nuno Gonçalves. Neural implicit morphing of face images. *arXiv preprint arXiv:2308.13888*, 2023.
- [21] Luiz Schirmer, Tiago Novello, Guilherme Schardong, Vinícius da Silva, Hélio Lopes, and Luiz Velho. How to train your (neural) dragon. In *Conference on Graphics, Patterns and Images, 36. (SIBGRAPI)*, 2023. URL <http://urlib.net/ibi/8JMKD3MGPEW34M/49T46US>.
- [22] Vincent Sitzmann, Julien Martel, Alexander Bergman, David Lindell, and Gordon Wetzstein. Implicit neural representations with periodic activation functions. *Advances in neural information processing systems*, 33:7462–7473, 2020.
- [23] Ying Song, Jiaping Wang, Li-Yi Wei, and Wencheng Wang. Vector regression functions for texture compression. *ACM Transactions on Graphics (TOG)*, 35(1):1–10, 2015.
- [24] Matthew Tancik, Pratul Srinivasan, Ben Mildenhall, Sara Fridovich-Keil, Nithin Raghavan, Utkarsh Singhal, Ravi Ramamoorthi, Jonathan Barron, and Ren Ng. Fourier features let networks learn high frequency functions in low dimensional domains. *Advances in Neural Information Processing Systems*, 33:7537–7547, 2020.
- [25] Zhijie Wu, Yuhe Jin, and Kwang Moo Yi. Neural fourier filter bank. In *Proceedings of the IEEE/CVF Conference on Computer Vision and Pattern Recognition*, pages 14153–14163, 2023.
- [26] Yiheng Xie, Towaki Takikawa, Shunsuke Saito, Or Litany, Shiqin Yan, Numair Khan, Federico Tombari, James Tompkin, Vincent Sitzmann, and Srinath Sridhar. Neural fields in visual computing and beyond. In *Computer Graphics Forum*, volume 41, pages 641–676. Wiley Online Library, 2022.
- [27] Guandao Yang, Serge Belongie, Bharath Hariharan, and Vladlen Koltun. Geometry processing with neural fields. *Advances in Neural Information Processing Systems*, 34:22483–22497, 2021.
- [28] Wang Yifan, Lukas Rahmann, and Olga Sorkine-hornung. Geometry-consistent neural shape representation with implicit displacement fields. In *International Conference on Learning Representations*, 2021.
- [29] Gizem Yüce, Guillermo Ortiz-Jiménez, Beril Besbinar, and Pascal Frossard. A structured dictionary perspective on implicit neural representations. In *Proceedings of the IEEE/CVF Conference on Computer Vision and Pattern Recognition*, pages 19228–19238, 2022.
- [30] Andreas Zell, Nuri Benbarka, Timon Hofer, and Hamd Ul Moqueet Riaz. Seeing implicit neural representations as fourier series. In *2022 IEEE/CVF Winter Conference on Applications of Computer Vision (WACV)*. IEEE Computer Society, 2022.

A Proofs of theorems

In this section, we prove Theorems 1 and 2. We consider the INR input to be 1D since the general case is analogous. Let $f(x) = \mathbf{L} \circ \mathbf{S} \circ \mathbf{D}(x)$ be a sinusoidal INR with $\mathbf{S}(\mathbf{x}) = \sin(\mathbf{W}\mathbf{x} + \mathbf{b})$, where $\mathbf{W} \in \mathbb{R}^{n \times m}$ is the hidden matrix, and $\mathbf{b} \in \mathbb{R}^n$ the bias. The input layer $\mathbf{D}(\mathbf{x}) = \sin(\omega\mathbf{x} + \varphi)$ projects the input x into a list of harmonics with frequencies $\omega = (\omega_1, \dots, \omega_m) \in \mathbb{R}^m$ and shifts $\varphi \in \mathbb{R}^m$. Finally, \mathbf{L} is a linear layer. The i th hidden neuron can be written as follows:

$$h_i(x) = \sin \left(\sum_{j=1}^m W_{ij} \sin(\omega_j x + \varphi_j) + b_i \right)$$

Note that, h_i receives a list of m input neurons $D_j(x) = \sin(\omega_j x + \varphi_j)$ that are combined with the weights W_{ij} and activated by \sin . Before presenting the expansion of h_i (Theorem 1), let us recall the (Fourier) expansion of a neuron with width 1 and no bias [1, Page 361]:

$$\sin(a \sin(x)) = \sum_{k \in \mathbb{Z} \text{ odd}} J_k(a) \sin(kx), \quad \text{with } J_k(a) = \int_0^\pi \cos(kt - a \sin(t)) dt. \quad (7)$$

The functions J_k are the *Bessel functions* of the first kind. The expansion of h_i generalizes (7). Its proof consists of verifying (1) as well as a similar formula using the cosine as the activation function:

$$\cos \left(\sum_{j=1}^m W_{ij} \sin(\omega_j x + \varphi_j) + b_i \right) = \sum_{\mathbf{k} \in \mathbb{Z}^m} \alpha_{\mathbf{k}} \cos(\langle \mathbf{k}, \omega x + \varphi \rangle + b_i). \quad (8)$$

Now, we present the proof of Theorem 1, that gives the harmonic expansion (1) of the neuron h_i ,

$$h_i(x) = \sum_{\mathbf{k} \in \mathbb{Z}^m} \alpha_{\mathbf{k}} \sin(\beta_{\mathbf{k}} x + \lambda_{\mathbf{k}}), \quad \text{with } \beta_{\mathbf{k}} = \sum_j k_j \omega_j, \quad \lambda_{\mathbf{k}} = \sum_j k_j \varphi_j + b_i, \quad \alpha_{\mathbf{k}} = \prod_{j=1}^m J_{k_j}(W_{ij}).$$

Proof. For simplicity, we denote W_{ij} by a_j . The proof is by induction in m . For the base case $m = 1$, we prove $\sin(a \sin(y) + b) = \sum_{k \in \mathbb{Z}} J_k(a) \sin(ky + b)$ with $y = \omega x + \varphi$. For this, we use the expansion in (7) and its cosine analogous expansion $\cos(a \sin(y)) = \sum J_l(a) \cos(ly)$, here the sum is over the even numbers. Thus, applying the trigonometric identity $\sin(a + b) = \sin(a) \cos(b) + \cos(a) \sin(b)$ we obtain:

$$\begin{aligned} \sin(a \sin(y) + b) &= \sin(a \sin(y)) \cos(b) + \cos(a \sin(y)) \sin(b) \\ &= \sum_{k \in \mathbb{Z} \text{ odd}} J_k(a) \sin(ky) \cos(b) + \sum_{l \in \mathbb{Z} \text{ even}} J_l(a) \cos(ly) \sin(b) \\ &= \sum_{k \in \mathbb{Z} \text{ odd}} J_k(a) \sin(ky + b) + \sum_{l \in \mathbb{Z} \text{ even}} J_l(a) \sin(ly + b) \\ &= \sum_{k \in \mathbb{Z}} J_k(a) \sin(ky + b). \end{aligned}$$

In the third equality we combined the formula $\sin(a) \cos(b) = \frac{\sin(a+b) + \sin(a-b)}{2}$ and the fact that $J_{-k}(a) = (-1)^k J_k(a)$ to rewrite the summations. The proof of the formula using the cosine as an activation function is similar.

Assume that the formulas hold for $m - 1$, with $m > 1$, we prove (1) holds for m (the induction step). Again, we denote $y_j = \omega_j x + \varphi_j$ and b_i as b for simplicity.

$$\sin \left(\sum_{j=1}^m a_j \sin(y_j) + b \right) = \sin \left(\sum_{j=1}^{m-1} a_j \sin(y_j) + b \right) \cos(a_m \sin(y_m)) \quad (9)$$

$$+ \cos \left(\sum_{j=1}^{m-1} a_j \sin(y_j) + b \right) \sin(a_m \sin(y_m)) \quad (10)$$

$$= \sum_{\mathbf{l} \in \mathbb{Z}^{m-1}, k \in \mathbb{Z} \text{ even}} \alpha_{\mathbf{l}} J_k(a_m) \sin(\langle \mathbf{l}, \mathbf{y} \rangle + b) \cos(k y_m) \quad (11)$$

$$+ \sum_{\mathbf{l} \in \mathbb{Z}^{m-1}, k \in \mathbb{Z} \text{ odd}} \alpha_{\mathbf{l}} J_k(a_m) \cos(\langle \mathbf{l}, \mathbf{y} \rangle + b) \sin(k y_m) \quad (12)$$

$$= \sum_{\mathbf{k} \in \mathbb{Z}^m} \alpha_{\mathbf{k}} \sin(\langle \mathbf{k}, \mathbf{y} \rangle + b) \quad (13)$$

We use the induction hypothesis in the second equality and an argument similar to the one used in the base case to rewrite the harmonic sum. Again, the cosine activation function case is analogous. \square

Yüce et al. [29] presented a similar formula for MLPs activated by polynomial functions. While it is evident that the sine function can be approximated by a polynomial using Taylor series, our formula requires no approximations. In addition to providing a simple proof, we also derive the analytical expressions for the amplitudes. These expressions enable us to compute upper bounds (Theorem 2) for the new frequencies $\alpha_{\mathbf{k}}$ in terms of \mathbf{k} and \mathbf{W} . Next, we prove such inequality,

$$|\alpha_{\mathbf{k}}| = \prod_{j=1}^m \left(\frac{|W_{ij}|}{2} \right)^{|k_j|} \frac{1}{|k_j|!}.$$

Proof. Again, we denote W_{ij} by a_j to simplify notation. Theorem 1 says that $\alpha_{\mathbf{k}} = \prod_{j=1}^m J_{k_j}(a_j)$. To estimate an upper bound for this number, we use the following inequality [15], which gives an upper bound for the Bessel functions $J_i(a)$.

$$|J_i(a)| < \frac{\left(\frac{|a|}{2}\right)^i}{i!}, \quad i > 0, \quad a > 0. \quad (14)$$

Observe that this inequality also holds for $a < 0$ since $|J_i(-a)| = |J_i(a)|$. Therefore, replacing (14) in $\prod_{j=1}^m J_{k_j}(a_j)$ and using $|J_{-i}(a)| = |J_i(a)|$ results in the desired inequality. \square

B Towards computing the Fourier series of a periodic INR

Here, we consider the INR f to have \mathbb{R}^2 as domain, however, it could be easily extended to other domains. Observe that a given frequency \mathbf{f} may appear several times as generated frequencies $\beta_{\mathbf{k}} = \mathbf{k}^\top \omega$ with different coefficients \mathbf{k} in the expansion (1). Here, we provide a characterization of all $\mathbf{k} \in \mathbb{Z}^m$ such that $\mathbf{k}^\top \omega = \frac{2\pi}{p} \mathbf{f}$, where p is the period of the sinusoidal network. This leads to an algorithm to compute the Fourier series of the periodic INR f .

To guarantee that a sinusoidal INR f initialized with $\omega = \frac{2\pi}{p} [\mathbf{f}_1, \mathbf{f}_2] \in \frac{2\pi}{p} \mathbb{Z}^{m \times 2}$ can represent an arbitrary image, we need to determine when it can reconstruct a given frequency $\mathbf{f} \in \mathbb{Z}^2$. This is equivalent to find a solution $\mathbf{k} \in \mathbb{Z}^m$ to the system of Diophantine equations

$$[\mathbf{f}_1, \mathbf{f}_2]^\top \mathbf{k} = \mathbf{f} \quad \text{for } \mathbf{f} \in \mathbb{Z}^2. \quad (15)$$

Let $\mathbf{B} = \mathbf{U} [\mathbf{f}_1, \mathbf{f}_2]^\top \mathbf{V}$ be the Smith normal form of $[\mathbf{f}_1, \mathbf{f}_2]^\top$. Assuming $\mathbf{e} = \mathbf{U} \mathbf{f}$ such that $e_i/B_{ii} \in \mathbb{Z}$ for $i = 1, 2$, then all integer solutions of (15) have the form $\mathbf{V} \left[\frac{e_1}{B_{11}} \frac{e_2}{B_{22}} l_1 \dots l_{m-2} \right]^\top$ with l_1, \dots, l_{m-2} arbitrary integers [11, Pg. 31].

Now, recall that we are considering $\omega_1 = \frac{2\pi}{p}(1, 0)$ and $\omega_2 = \frac{2\pi}{p}(0, 1)$, thus the Smith normal form and unimodular matrices \mathbf{U}, \mathbf{V} are given by,

$$\mathbf{B} = [\mathbb{I}_2 \mid \mathbf{0}_{2 \times m-2}], \quad \mathbf{U} = \mathbb{I}_2, \quad \text{and} \quad \mathbf{V} = \left[\begin{array}{c|c} \mathbb{I}_2 & \begin{matrix} -f_{13} & \dots & -f_{1m} \\ -f_{23} & \dots & -f_{2m} \end{matrix} \\ \hline \mathbf{0}_{m-2 \times 2} & \mathbb{I}_{m-2} \end{array} \right].$$

Then $\mathbf{e} = \mathbf{f}$ and the divisibility condition is satisfied since $B_{ii} = 1$. Therefore, any frequency $\mathbf{f} \in \mathbb{Z}^2$ can be represented by f , and the integer solutions of (15) are given by

$$\mathbb{K}(\mathbf{f}) = \left\{ \left[\begin{array}{c} \mathbf{f}_1 - \sum_{k=1}^{m-2} l_k \mathbf{f}_{1,k+2} \\ \mathbf{f}_2 - \sum_{k=1}^{m-2} l_k \mathbf{f}_{2,k+2} \\ l_1 \\ \vdots \\ l_{m-2} \end{array} \right] : l_1, \dots, l_{m-2} \in \mathbb{Z} \right\}.$$

Using $\mathbb{K}(\mathbf{f})$ and (3), we obtain the Fourier series of f by aggregating all coefficients associated with each frequency $\mathbf{f} \in \mathbb{Z}^2$. That is, the Fourier coefficients are given by $\hat{A}_{\mathbf{f}} = \sum_{\mathbf{k} \in \mathbb{K}(\mathbf{f})} \langle \mathbf{C}, A_{\mathbf{k}} \rangle$ and $\hat{B}_{\mathbf{f}} = \sum_{\mathbf{k} \in \mathbb{K}(\mathbf{f})} \langle \mathbf{C}, B_{\mathbf{k}} \rangle$. To find a similar formula for the general case of $\omega \in \mathbb{R}^{m \times d}$, we must consider $\omega_i = \mathbf{e}_i$ for $i = 1, \dots, d$. Then, the aggregation of coefficients is analogous.

C On the sub-periodicity of sinusoidal INRs

Observe that initializing a sinusoidal INR f using input neurons with period p implies that f is also periodic with period p (Theorem 1). However, the initialization could force the INR to have sub-periods. In that case, it would never be able to fit a signal with fundamental period p . We derive a condition to avoid such a problem. First, recall that Theorem 1 says that a hidden neuron $h(\mathbf{x}) = \sin(\mathbf{W}_i \sin(\omega \mathbf{x} + \varphi) + b_i)$, with $\omega = \frac{2\pi}{p} [\mathbf{f}_1, \mathbf{f}_2]$ for some $\mathbf{f}_1, \mathbf{f}_2 \in \mathbb{Z}^m$, can be expressed as:

$$h(\mathbf{x}) = \sum_{\mathbf{k} \in \mathbb{Z}^m} \alpha_{\mathbf{k}} \sin(\beta_{\mathbf{k}} \mathbf{x} + \lambda_{\mathbf{k}}) \quad (16)$$

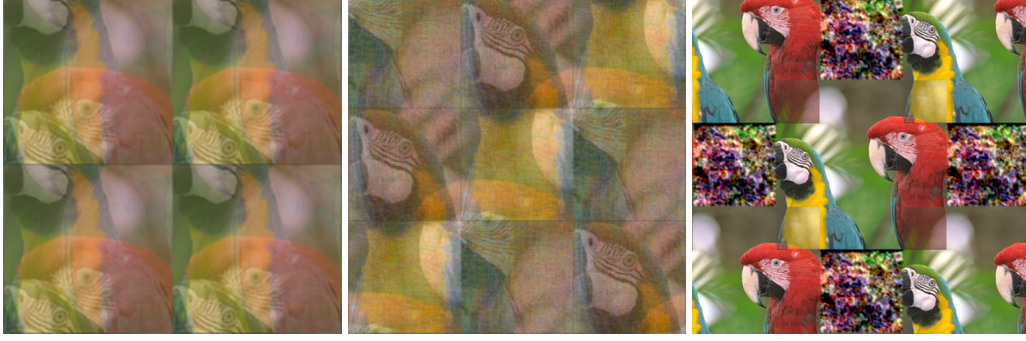
with frequencies and phase-shifts given by $\beta_{\mathbf{k}} = \mathbf{k}^\top \omega$ and $\lambda_{\mathbf{k}} = \mathbf{k}^\top \varphi + b_i$. Therefore, $\beta_{\mathbf{k}} \mathbf{x} = \frac{2\pi}{p} (\langle \mathbf{k}, \mathbf{f}_1 \rangle x + \langle \mathbf{k}, \mathbf{f}_2 \rangle y)$. Now, suppose that h has sub-period $\frac{p}{q}$ in x -axis and $\frac{p}{s}$ in y -axis ($q, s \in \mathbb{Z}^+$), that is, $h(x, y) = h(x + \frac{p}{q}, y + \frac{p}{s})$. However, (16) implies

$$h\left(x + \frac{p}{q}, y + \frac{p}{s}\right) = \sum_{\mathbf{k} \in \mathbb{Z}^m} \alpha_{\mathbf{k}} \sin\left(\beta_{\mathbf{k}} \mathbf{x} + \lambda_{\mathbf{k}} + 2\pi \left\langle \mathbf{k}, \frac{\mathbf{f}_1}{q} + \frac{\mathbf{f}_2}{s} \right\rangle\right). \quad (17)$$

Thus, since $\sin(x + 2\pi k) = \sin(x)$ for $k \in \mathbb{Z}$, we have that Expansions 16 and 17 are equal only if $\left\langle \mathbf{k}, \frac{\mathbf{f}_1}{q} + \frac{\mathbf{f}_2}{s} \right\rangle \in \mathbb{Z}$ for all $\mathbf{k} \in \mathbb{Z}^m$. Therefore, h (and consequently f) has sub-periods only if there exists $q > 1$ or $s > 1$ such that $\frac{\mathbf{f}_1}{q} + \frac{\mathbf{f}_2}{s} \in \mathbb{Z}^m$.

An important consequence of our initialization is that the addition of the input frequencies $(1, 0), (0, 1)$ to $[\mathbf{f}_1, \mathbf{f}_2]$ prevents the appearance of sub-periods. Indeed, we define the first elements of $[\mathbf{f}_1, \mathbf{f}_2]$ as $f_{11} = 1, f_{21} = 0, f_{12} = 0$, and $f_{22} = 1$. Hence, this implies that $\frac{f_{11}}{q} + \frac{f_{21}}{s} = \frac{1}{q} \in \mathbb{Z}$ if and only if $q = 1$, and $\frac{f_{12}}{q} + \frac{f_{22}}{s} = \frac{1}{s} \in \mathbb{Z}$ if and only if $s = 1$.

Fig 13 illustrates three cases where the choice of the input frequencies ω results in a bad reconstruction: (a) $[\mathbf{f}_1, \mathbf{f}_2]$ with odd frequencies and period $p = 2$; (b) $[\mathbf{f}_1, \mathbf{f}_2]$ defined by the cartesian product of $\{1, 10, 100\}$ and $p = 2$, and (c) $[\mathbf{f}_1, \mathbf{f}_2]$ with odd frequencies and period $p = 3$. Fig 13c shows that in the case $p = 3$ there is an overlap of copies generated by the periodicity. This suggests an inconsistency between the selected period p and the resulting period of f . Adding the frequencies $(0, 1)$ and $(1, 0)$ solves this problem, see Fig 5 in the main text.



(a) ω defined with odd frequencies. (b) $\omega = \{(u, v) | u, v \in \pm[1, 10, 100]\}$ (c) Extrapolation to $[-2, 2]$ of f with ω as in (a) and $p = 3$.

Figure 13: Bad reconstructions given by specific (wrong) initializations of the input frequencies.

D Extension of Theorem 1 to deeper networks

This section extends Theorem 1 to multiple hidden layers. By recursively applying the argument from the proof of the theorem, we can establish the generalization using induction. We demonstrate the case of an INR with two hidden layers for simplicity, however, the general case is analogous.

Let $f(\mathbf{x}) = \mathbf{L} \circ \mathbf{S}_1 \circ \mathbf{S}_0 \circ \mathbf{D}(\mathbf{x})$ with $\mathbf{S}_i(\mathbf{x}) = \sin(\mathbf{W}^{(i)}\mathbf{x} + \mathbf{b}^{(i)})$. Then, a neuron of the last hidden layer can be written as $h(\mathbf{x}) = \sin(\mathbf{a} \sin(\mathbf{W}^{(0)} \sin(\omega\mathbf{x} + \varphi) + \mathbf{b}^{(0)}) + b^{(1)})$, where \mathbf{a} is a row of the hidden matrix $\mathbf{W}^{(1)}$. Observe that by denoting $\mathbf{y}^{(0)} = \mathbf{W}^{(0)} \sin(\omega\mathbf{x} + \varphi) + \mathbf{b}^{(0)}$ we can apply (13) as in the case $d = 1$ as follows:

$$h(\mathbf{x}) = \sin\left(\sum_{i=1}^n a_j \sin(y_i^{(0)}) + b^{(1)}\right) = \sum_{\mathbf{l} \in \mathbb{Z}^n} \alpha_{\mathbf{l}}^{(1)} \sin(\langle \mathbf{l}, \mathbf{y}^{(0)} \rangle + b^{(1)})$$

where $\alpha_{\mathbf{l}}^{(1)} = \prod_{i=1}^n J_{l_i}(a_i)$. When replacing the term $\mathbf{y}^{(0)}$ in the sine of the last expression, it can be written as a composition of sines:

$$\begin{aligned} \sin(\langle \mathbf{l}, \mathbf{y}^{(0)} \rangle + b^{(1)}) &= \sin\left(\sum_{j=1}^m \langle \mathbf{l}, \mathbf{W}_{*j}^{(0)} \rangle \sin(\omega_j \mathbf{x} + \varphi_j) + \langle \mathbf{l}, \mathbf{b}^{(0)} \rangle + b^{(1)}\right) \\ &= \sum_{\mathbf{k} \in \mathbb{Z}^m} \alpha_{\mathbf{k}}^{(0)} \sin(\langle \mathbf{k}, \omega \rangle \mathbf{x} + \langle \mathbf{k}, \varphi \rangle + \langle \mathbf{l}, \mathbf{b}^{(0)} \rangle + b^{(1)}) \end{aligned}$$

Here, $\alpha_{\mathbf{k}}^{(0)} = \prod_{j=1}^m J_{k_j}(\langle \mathbf{l}, \mathbf{W}_{*j}^{(0)} \rangle)$. The first equality is obtained by substituting $\mathbf{y}^{(0)}$ and aggregating the terms appropriately, the second one is given, again, by (13) used in the proof of Theorem 1. Then, denoting $\alpha_{\mathbf{k}, \mathbf{l}} = \alpha_{\mathbf{l}}^{(1)} \alpha_{\mathbf{k}}^{(0)}$ and $\lambda_{\mathbf{k}, \mathbf{l}} = \langle \mathbf{k}, \varphi \rangle + \langle \mathbf{l}, \mathbf{b}^{(0)} \rangle + b^{(1)}$ we obtain the desired equality:

$$h(\mathbf{x}) = \sum_{(\mathbf{l}, \mathbf{k}) \in \mathbb{Z}^n \times \mathbb{Z}^m} \alpha_{\mathbf{k}, \mathbf{l}} \sin(\langle \mathbf{k}, \omega \rangle \mathbf{x} + \lambda_{\mathbf{k}, \mathbf{l}}) \quad (18)$$

Observe that several properties drawn from the case of an INR with a single hidden layer hold for the general case. First, the amplitudes $\alpha_{\mathbf{k}, \mathbf{l}}$ depend only on the hidden matrices, and still product of Bessel functions. On the other hand, only the biases of the model influence the shifts $\lambda_{\mathbf{k}, \mathbf{l}}$. This may imply that not all biases are necessary during training.

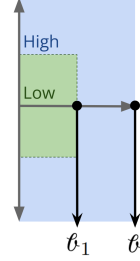
We emphasize that adding more hidden layers doesn't introduce new frequencies, as they are, once again, defined by $\langle \mathbf{k}, \omega \rangle$. Then, deep sinusoidal networks just fine tune the amplitudes of the generated frequencies, which are completely determined by the choice of ω .

E Additional experiments

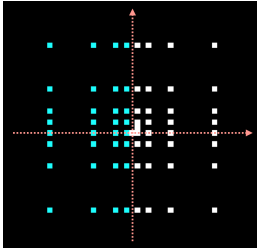
E.1 Initialization in the half cube

We showed that initializing a frequency ω_i implies that its negative $-\omega_i$ also appears in the spectrum. Here, we use this fact to avoid sampling duplicated frequencies in $[-\ell, \ell]^2$ to obtain a better reconstruction. We test the capacity of two INRs with the same architecture $m = 102, n = 512$, but with different initializations for their frequencies ω (blue and white dots in Fig 14a) and ω' (white/green dots in Fig 14b):

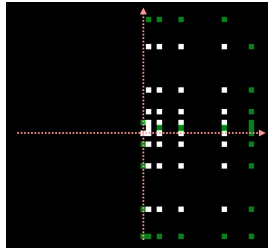
$$\omega = [(k, l) \mid k, l \in \{1, 3, 4, 7, 10, 20\}] \text{ and } \omega' = [(k, l) \mid (k, l) \in \omega \text{ with } k > 0] \sqcup \eta.$$



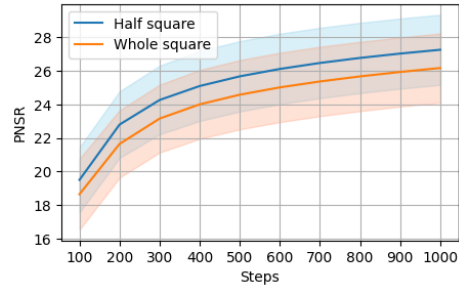
Where η are additional frequencies (in green) sampled in the Cartesian product of the list $[0, 1, 2, 3, 4, 7, 10, 20]$. Fig 14c shows the PSNR of the resulting networks with respect to the iterations. The results show that adding the new frequencies η results in a slight but consistent improvement in the PSNR during training.



(a) Initialization of ω in the square. The blue dots are the negative frequencies of those in white.



(b) Initialization of ω' in the half square. The frequencies in green replace the frequencies in blue.



(c) Comparison of PSNR in both initializations of input frequencies during training.

Figure 14: Comparison of reconstructions with different input frequency initializations.

E.2 Initialization of hidden layer

In Section 4.2 we proposed an initialization for the hidden matrix \mathbf{W} . The following experiment shows that an initialization that considers the bounding limit for \mathbf{W} may grant a faster convergence. In Fig 15, we initialize the INRs of size $m = 416, n = 1024$ with bandlimit $\ell = 82$ and bounds $c_1 = 1.0, c_2 = 0.2$. The INR trains during only 10 epochs to observe the speed of convergence and fits an image with resolution 1024^2 . Observe that the INRs that considered the bounds to initialize their hidden layer \mathbf{W} (2^o row) present a better reconstruction. This can also be observed in the zoom-ins of images, where our method presents more details.

E.3 Learned bounds

In Section 4.2 we presented a novel scheme to bound the sinusoidal INR during training. Furthermore, we also proposed an architecture that allows us to learn those bounds during training. In this section, we analyze the coherence of the resulting bounds as we vary the signal bandlimit.

We define several INRs with size $m = n = 416$, initial bounds with value 0.5 and bandlimits $\ell = 34, 85, 171, 256$. Then, we fit them to images with resolution 512^2 using our scheme of learnable bounds. Fig 16 shows the bounds trained after 400 epochs. Note that all plots have a green, dashed line that divides frequencies into low (L) and high (H).

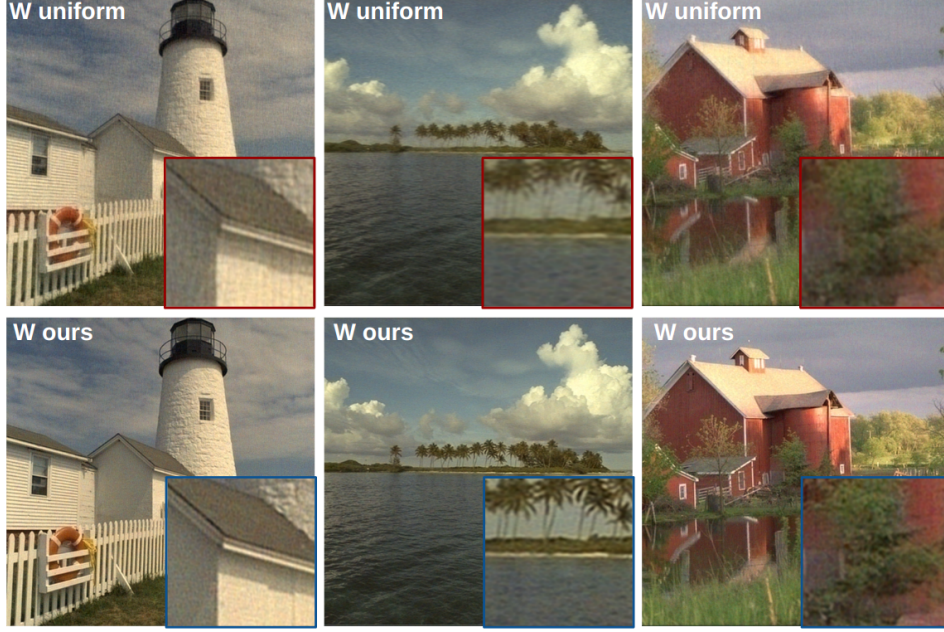


Figure 15: Comparison between INRs with different initializations for \mathbf{W} . The 1^o and 2^o rows show the results of INRs initialized \mathbf{W} as usual (see [22]) and as proposed in Section 4.2, respectively. They were trained during 10 epochs to show the difference in convergence. The blue and red squares present a 6-times zoom-in of the image center.

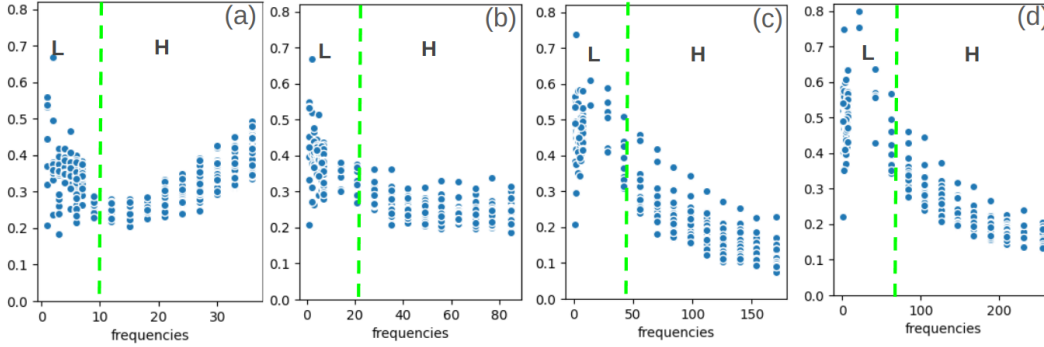


Figure 16: Ablation of the learned bounds of each column. The X axis corresponds to the maximum coordinate (in absolute value) of the frequency ω_j , while the Y axis shows the trained bound ϵ_j of \mathbf{W} 's j -th column. Thus, the blue points in the diagram represent $(\max(\omega_j), \epsilon_j)$.

Observe that in Fig 16a the low frequencies are saturated around a height of 0.37, showing that their use is reduced from the initial 0.5. Conversely, the amplitude of frequencies in \mathbf{H} increases as the frequency gets higher. This shows that the INR finds it necessary to increase the amplitudes of high frequencies for a good reconstruction. For the case when $\ell = 85$ (Fig 16b), training started discriminating which of the low frequencies contributes more to the reconstruction; this is observed by the spreading of bounds. As for the high frequencies, we observe a more uniform behavior, which may indicate that all frequencies may be contributing the same amount of information during training. This is also an indicator that the parameter $\ell = 85$ ($B/3$) is a good bandlimit to train the INR.

Now, in Fig 16c-d, we can observe even more extreme behaviors. Low frequencies exhibit multiple distinct bounds, while high frequencies are suppressed to prevent noise generation. The patterns depicted in the figures align with our theory, confirming that we are effectively learning a bound that serves as a mechanism for spectral control.